6-1-2020

A Study of a Magnetic Cloud Propagating Through Large-Amplitude Alfven Waves

Charlie J. Farrugia
University of New Hampshire, Charlie.Farrugia@unh.edu

Noe Lugaz
University of New Hampshire, Noe.Lugaz@unh.edu

Bernard J. Vasquez
University of New Hampshire, bernie.vasquez@unh.edu

L. B. Wilson III
NASA Goddard Space Flight Center

WenYuan Yu
University of New Hampshire, Wenyuan.Yu@unh.edu

See next page for additional authors

Recommended Citation

Farrugia, C. J., Lugaz, N.,Vasquez, B. J., Wilson, L. B.,Yu, W., Paulson, K., et al. (2020).A study of a magnetic cloudpropagating through large-amplitudeAlfvén waves. Journal ofGeophysical Research: Space Physics,125, e2019JA027638. https://doi.org/10.1029/2019JA027638

JGR Space Physics

RESEARCH ARTICLE
10.1029/2019JA027638

Key Points:
- Large-amplitude Alfvén waves are reported in the sheath of a magnetic cloud
- Reconnection at a discontinuity in the cloud sheath is followed by a slow expansion fan
- Magnetic cloud has an untypical orientation and is not force free

Correspondence to:
C. J. Farrugia,
charlie.farrugia@unh.edu

Citation:
Farrugia, C. J., Lugaz, N., Vasquez, B. J., Wilson, L. B., Yu, W., Paulson, K., et al. (2020). A study of a magnetic cloud propagating through large-amplitude Alfvén waves. *Journal of Geophysical Research: Space Physics*, *125*, e2019JA027638. https://doi.org/10.1029/2019JA027638

Received 13 NOV 2019
Accepted 28 APR 2020
Accepted article online 14 MAY 2020

A Study of a Magnetic Cloud Propagating Through Large-Amplitude Alfvén Waves

C. J. Farrugia[1], N. Lugaz[1], B. J. Vasquez[1], L. B. Wilson III[2], W. Yu[1], K. Paulson[3], R. B. Torbert[1], and F. T. Gratton[4]

[1]Space Science Center, University of New Hampshire, Durham, NH, USA, [2]NASA Goddard Space Flight Center, Greenbelt, MD, USA, [3]Harvard-Smithsonian Center for Astrophysics, Cambridge, MA, USA, [4]National Academy of Science of Buenos Aires, Buenos Aires, Argentina

Abstract We discuss *Wind* observations of a long and slow magnetic cloud (MC) propagating through large-amplitude Alfvén waves (LAAWs). The MC axis has a strong component along GSE X, as also confirmed by a Grad-Shafranov reconstruction. It is overtaking the solar wind at a speed roughly equal to the upstream Alfvén speed, leading to a weak shock wave 17 hr ahead. We give evidence to show that the nominal sheath region is populated by LAAWs: (i) a well-defined de Hoffmann-Teller frame in which there is excellent correlation between the field and flow vectors, (ii) constant field and total pressure, and (iii) an Alfvén ratio (i.e., ratio of kinetic-to-magnetic energy of the fluctuations) near unity at frequencies much lower than the ion cyclotron frequency in the spacecraft frame. In the region where the LAAWs approach the MC's front boundary there are field and flow discontinuities. At the first, magnetic reconnection is taking place, as deduced from a stress balance test (Walén test). This severs connection of some field lines to the Sun and the solar wind strahl disappears. There follows a 2-hr interval where the magnetic field strength is diminished while pressure balance is maintained. Here the bidirectionality of the suprathermal electron flows is intermittently disrupted. This interval ends with a slow expansion fan downstream of which there is a dropout of halo electrons just inside the front boundary of the MC. This study illustrates an untypical case of a slow MC interacting with LAAWs in the slow solar wind.

1. Introduction

Two salient features in the solar wind are (i) large-amplitude fluctuations with correlated fluctuating velocities $\delta\mathbf{V}$ and magnetic fields $\delta\mathbf{B}$, and (ii) magnetic clouds (MCs), containing a slow and large rotation of the magnetic field vector and high magnetic field strength. These two features are normally not observed in association with each other.

The correlated fluctuations usually exhibit some aspects of Alfvén wave modes and are thus called Alfvénic fluctuations. Alfvénic fluctuations are observed most often in high-speed streams and have periods of hours (e.g., Belcher & Davis Jr, 1971; Matthaeus & Goldstein, 1982). In low-speed streams Alfvénic fluctuations are intermittent and have smaller amplitudes. On the trailing edges of the high-speed streams and closer to the Sun, the degree of correlation can approach that predicted for Alfvén wave modes moving in the same direction along the interplanetary magnetic field. Even at 1 AU, fluctuations can, at times, closely satisfy the Walén relation $\delta\mathbf{V} = \pm\delta\mathbf{B}/(4\pi\rho)^{1/2}$ where ρ is the mass density (e.g., Chao et al., 2014; Wang et al., 2012). The sign of the relation and the direction of the interplanetary magnetic field are consistent with fluctuations that propagate away from the Sun from where they presumably originate (e.g., Belcher & Davis Jr, 1971). The high-speed streams in which the fluctuations are embedded have been clearly identified as coming from coronal holes at the Sun (e.g., Levine et al., 1977).

MCs result from eruptive phenomena on the Sun. They were first identified as magnetic loops following an interplanetary shock from measurements by a group of spacecraft separated both radially and longitudinally (Burlaga et al., 1981). They have since been studied intensively, in part because the presence of a negative GSM B_z of long duration in a subset of these gives rise to intense, repetitive geomagnetic substorms and strong storm activity (e.g. Farrugia et al., 1993, 1997, 2013). Many MCs expand as they travel antisunward. They are known to occur in association with filament eruptions at the Sun and originate in association with the streamer belt. This, then, gives MCs, and solar ejecta in general, a source region that differs from the

coronal holes from which high-speed streams emanate. As a result, the large-amplitude Alfvén waves that are usually found in high-speed streams are not expected to be located in front of the MCs and solar ejecta. Heinemann et al. (2019) gives one of the few cases where a solar ejecta originates close enough to a coronal hole that the in situ measurements show a mix of coronal hole and ejecta material.

In this paper we present what is, to the best of our knowledge, the first case in the ecliptic plane of a MC progressing in an ambient solar wind containing large-amplitude Alfvén waves. The preceding solar wind is a low-speed stream but contains large-amplitude Alfvénic fluctuations. Only a weak, evanescent/forming shock has been generated ahead of the MC. The sheath-like region ahead of the cloud contains large-amplitude fluctuations with properties closely corresponding to Alfvén wave modes. Cloud passage lasts for about 43 hr. The MC has an unusual orientation, with the axis of the flux rope subtending only a small angle to the Sun-Earth direction. We show that the ongoing interaction of the waves with the MC results in a number of discontinuities at one of which there is evidence of magnetic reconnection. Here the field-aligned electron strahl (beam) disappears. This is followed by an interval where the magnetic field is strongly depressed while pressure balance is maintained. Here the bidirectionality of solar wind suprathermal and field-aligned strahl electrons is intermittently disrupted. This period ends in a slow expansion fan behind which the density drops by more than an order of magnitude and the field strength rises. Here there is a depletion of halo electrons as the front boundary of the ejecta is crossed.

The layout of the paper is as follows. In section 2 we describe the *Wind* spacecraft instruments from which the data were acquired. We start section 3 with a brief overview of the observations. We then analyze successively the MC, the sheath region containing the LAAWs, and the interaction region between the waves and the MC. We end with a discussion section and our conclusions.

2. Instruments

We shall use magnetic field data from the Magnetic Field Investigation (MFI; Lepping et al., 1995) and plasma parameters from the Wind 3D Plasma Analyzer (3DP; Lin et al., 1995), both at 3-s resolution, and the Solar Wind Experiment (SWE; Ogilvie et al., 1995), where the resolution varies. For electrons we shall use new data obtained from recent state-of-the-art modeling of the electron velocity distribution functions (VDFs; see https://github.com/lynnbwilsoniii/wind_3dp_pros for more information and publicly available software). We recall that the velocity distribution of solar wind electrons may be divided into a low-energy core and a higher-energy suprathermal tail, with a break at about ~30–50 eV (Feldman et al., 1975; see also; Wilson III et al., 2019b). The suprathermal tail itself consists of two components, a field-aligned beam, called "strahl" (Rosenbauer et al., 1977), and a more diffuse, isotropic "halo." The new electron velocity moments derived from this analysis technique contain information on all three electron components (Wilson III et al., 2019a). The MFI is a boom-mounted dual triaxial fluxgate magnetometer. The 3DP instrument consists of six different sensors. There are two electron (EESA) and two ion (PESA) electrostatic analyzers with different geometrical factors and field-of-views covering the energy range from 3 eV to 30 keV. There are also a pair of solid state telescopes (SST) that measure electrons with energies up to 400–600 keV (depending on mode of operation) and protons with energies up to 6 MeV. SWE consists of two Faraday cup (FC) sensors and a vector electron and ion spectrometer (VEIS). The energy/charge range of the Faraday cups is 150 V to 8 kV, and that of the VEIS is 7 V to 24.8 kV. Data from *Wind* are mostly from the NASA CDAWeb site, but the electron data were taken from the Level 0 data products at http://sprg.ssl.berkeley.edu/wind3dp/data/wi/3dp/lz/ and calibrated specifically for this interval.

3. Observations

Figure 1 shows magnetic field and plasma observations from *Wind* for the interval 6 UT, 3 February, to 24 UT, 5 February 1998. (For simplicity, we shall henceforth denote hh:mm UT, 4 February 1998 by hh:mm UT (4).) The data are plotted in GSE coordinates. The average position of the spacecraft during this interval is (236, 3, −29) R_E (GSE). A large structure is encountered in the interval bracketed by the two magenta lines. During this time the magnetic field peaks at high values and the **B** vector executes a slow and large rotation (first four panels). Further, the proton temperature (Panel 6) is generally below that expected from normal solar wind expansion (blue trace; Lopez, 1987) and the proton beta β_p is below unity (last panel). These are features which define the structure as a MC (Burlaga et al., 1981). A few things to note are as follows: (i) The MC has an untypically long duration of 42.5 hr (4:30 UT (4) to 22 UT (5)). (ii) In the last

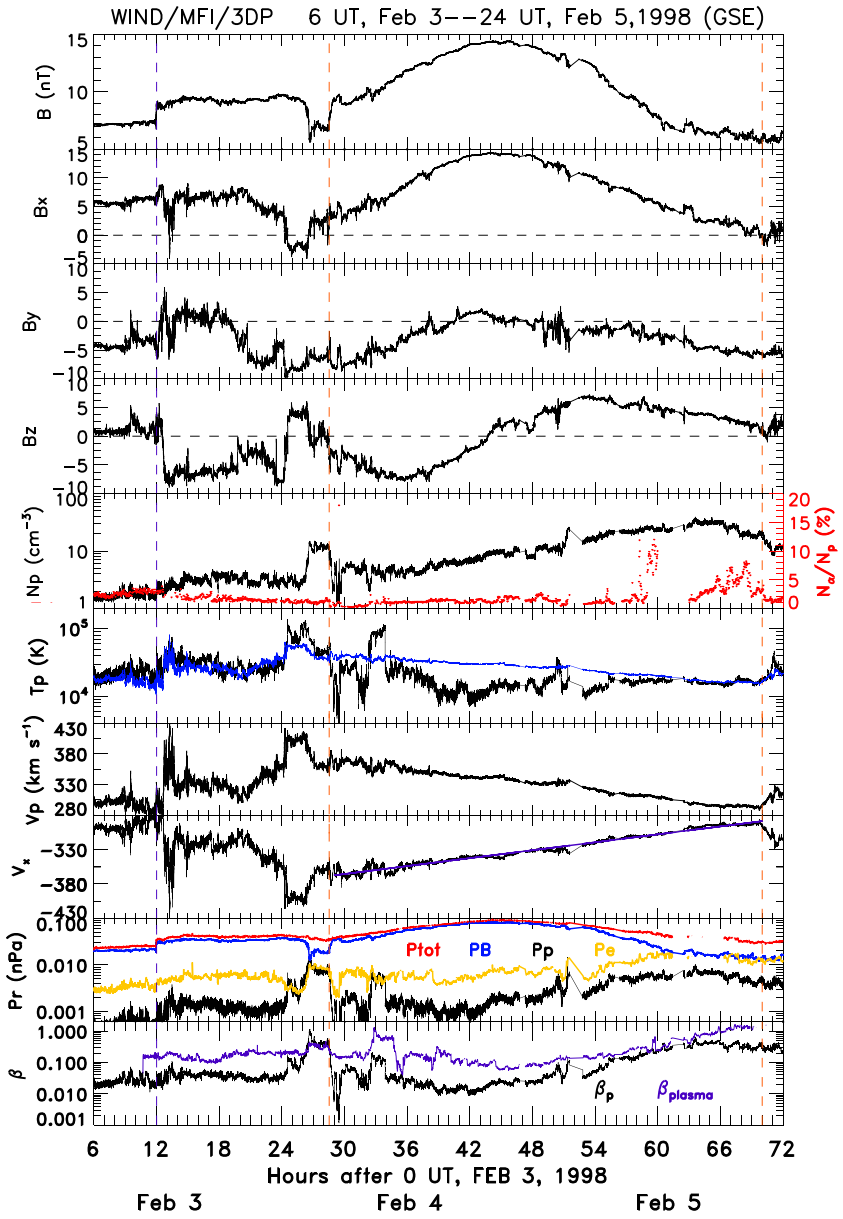

Figure 1. Magnetic field and plasma observations from *Wind* for the period 6 UT, 3 February, to 24 UT, 5 February 1998. From top to bottom: the total field, and its GSE components, the density (overlaid in red, the α particle-to-proton number density ratio in percent), the proton temperature (in blue, the expected temperature for normal solar wind expansion), the proton bulk speed, V_x with a linear fit in the MC interval, the proton (black), magnetic (blue), electron (yellow), and total (red) pressures, and the β_p. The vertical magenta lines bracket the magnetic cloud interval and the purple line is drawn at the weak shock wave ~17.5 hr ahead of it.

several hours the β_p increases significantly, mainly due to an increase in the density, so that the structure cannot be considered force-free since pressure gradients are important. (iii) Because the electron pressure, P_e (yellow trace in the last-but-one panel) is higher than the proton pressure, P_p, the plasma β even goes above unity (purple trace in the last panel). (iv) The magnetic field component executing a bipolar variation is that perpendicular to the ecliptic plane (B_z), and the one which peaks toward the center is B_x. From this one can expect a departure from the fairly common, east-west orientation of the flux rope axes of MCs, as we shall see below. (v) With an average speed of ~334 km/s, this is a very slow cloud. The declining profile of the bulk velocity indicates a radial expansion at the rate of ~29 km/s. We can express this expansion rate in terms of the normalized expansion parameter, ζ. This nondimensional parameter is defined as $\zeta = \frac{\Delta V_x}{\Delta t}\frac{D}{V_c^2}$, where Δt = duration of speed decrease, $\Delta V_x = V_x(in) - V_x(out)$ based on a linear fit of the V_x profile as a

function of time, D is the heliospheric distance (here, 1 AU), and V_c is the mean speed of the cloud (Démoulin et al., 2008; Gulisano et al., 2010). It can be shown that parameter ζ does not depend on Δt, V_c, or D. It assumes, however, different values for MCs which are not perturbed by the surrounding solar wind and those which are, that is, for example, those interacting with a trailing, faster stream. In our case, the linear fit gives $V_x = -423.07 + 1.92 \times t$. This fit is plotted by the purple trace in the eighth panel. Parameter $\zeta = 0.74$, which represents a borderline value between those obtained for perturbed and nonperturbed MCs (Gulisano et al., 2010).

The velocity of the front boundary of the cloud is 360 km/s so that it is overtaking the upstream solar wind by a speed which is comparable to the Alfvén speed in the upstream medium. Hence, there might be a very weak shock wave and, indeed, a shock wave-like disturbance is seen about 17 hr ahead of the MC, at ~12 UT (3) (blue line). The compression of the B field there is very weak: ~1.23, so the shock wave is practically evanescent or just forming.

The central observation of this paper occurs behind this shock wave in what is nominally the sheath region. In this case, there are large-amplitude changes in the magnetic field, which continue at fairly constant B and N for many hours until close to the MC front boundary. When we include also the velocity components, we shall show that these field and flow perturbations are consistent with their being large-amplitude Alfvén waves (LAAWs) (see discussion of Figure 5 below).

The inner sheath region is marked by two field and flow directional discontinuities (DDs) before the MC is encountered. At the first, at ~0 UT (4), there is a rotation in the all magnetic field components and polarity reversal in B_x and B_z (and the corresponding flow components, see below), which takes place at constant field strength, B. Here there occurs a burst of higher-speed flow (Panel 7). About 2.5 hr later, there is a ~2-hr interval of a weakened magnetic field accompanied by a rise in density and a drop in temperature, keeping the total pressure approximately constant (red trace in Panel 8). Finally, just inside the cloud there is a sharp drop in temperature and density at a small magnetic field rise. As we discuss later, an electron halo depletion is also present here. In the rest of the paper, we shall discuss in sequence the MC, its sheath region populated with LAAWs, and the interaction region with the MC where these DDs occur.

3.1. The MC

We first present an analysis of the MC. To determine the orientation of its axis, we carried out a minimum variance analysis (Sonnerup & Scheible, 1998) of the interval between the magenta lines in Figure 1. This routine returned a very robust result with a intermediate-to-minimum eigenvalue ratio of 22.0. The maximum variance direction is (0.876, 0.483, 0.010) (GSE), and we take this to be the cloud axis (see below). It is pointing mainly in the X and Y directions with a small inclination to the ecliptic plane: longitude (measured from the X axis) = 36°, latitude = 0.6°. Using the maximum variance direction as the axis of the MC is somewhat unusual (but see Xiao et al., 2004, discussed further in section 4) and needs some justification.

We now do an independent check and carry out a Grad-Shafranov reconstruction (Hu & Sonnerup, 2001, 2002). This approach is valid for any magnetohydrostatic structure with an invariant direction (i.e., an axis) and does not require the structure to be force free. We first transform the magnetic field and plasma data to the comoving de Hoffmann-Teller frame where the flow is field aligned (deHoffmann & Teller, 1950)). This is done by minimizing the convective electric field, $-\mathbf{v} \times \mathbf{B}$ (Khrabrov & Sonnerup, 1998). In this frame the condition for magnetohydrostatic equilibrium, that is, $\mathbf{j} \times \mathbf{B} = -\nabla P$, can be expressed by the Grad-Shafranov equation, which gives a relation between the vector potential A, the axial field B_z, and the sum of the thermal and axial magnetic pressure (i.e., the transverse pressure P_t). With the magnetic field expressed as

$\mathbf{B} = (\frac{\partial A}{\partial y}, \frac{-\partial A}{\partial x}, B_z)$, we have

$$\frac{\partial^2 A}{\partial x^2} + \frac{\partial^2 A}{\partial y^2} = -\mu_0 \frac{d}{dA}\left(P + \frac{B_z^2}{2\mu_0}\right) = -\mu_0 \frac{dP_t(A)}{dA}. \quad (1)$$

It can be shown (Sturrock, 1994) that the transverse pressure $P_t(A)$ is a function of A only. We then require that P_t be single valued, and from this condition we obtain the axis orientation of the flux rope and the closest distance the spacecraft passes from it (i.e., the impact parameter). This is done by doing a polynomial fit to P_t(A). The associated fitting residue, R_f, gives a measure of the quality of the fit. Typically, the GS reconstruction is good up to a distance which is less than the radius inferred from the data.

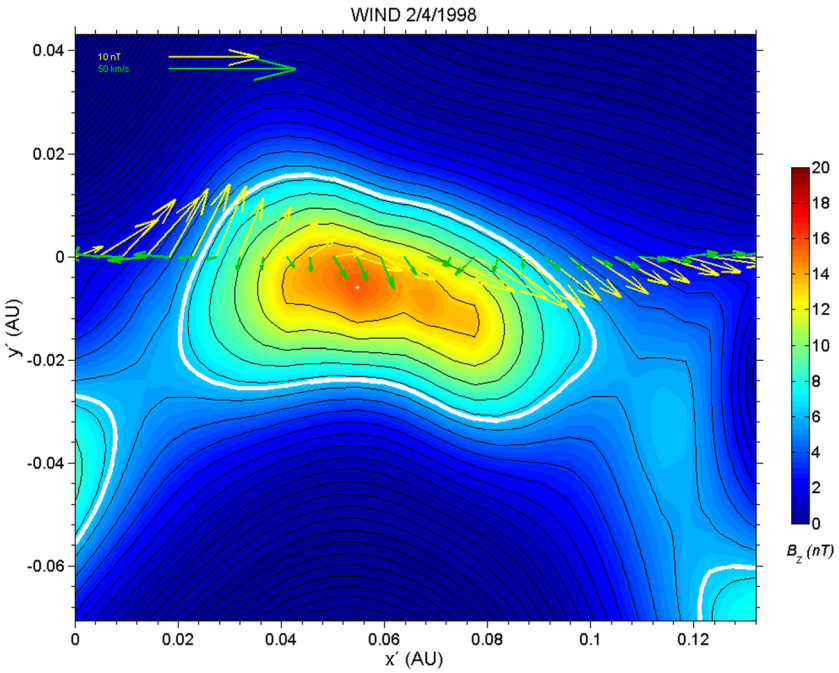

Figure 2. Magnetic contour map obtained from Grad-Shafranov (GS) reconstruction. The contour lines give the direction of the magnetic field in a plane perpendicular to the cloud axis. The color scheme shows the out-of-plane (axial) field strength. The white dot is where the axial field strength maximizes. The arrows are sample field (yellow) and flow (green) vectors along the spacecraft trajectory. The thick white curve is the boundary of the MC as determined by the GS method.

The best fit of P_t(A) gives the right-hand side of the Grad-Shafranov Equation (1). We then employ a Grad-Shafranov solver to solve Equation (1) by Taylor expanding the solution away from the spacecraft trajectory. The resulting solution is a magnetic field map which is presented in the transverse *XY* plane as closed contours of A.

Figures 2 and 3 present the results. Figure 2 shows the contours of the magnetic field in the plane perpendicular to the axis. The colors give the strength of the axial field, B_z, according to the color scheme on the right. The structure has an elongated cross section. The thick white curve is the boundary as determined by the algorithm. The arrows show measurements of **B** (yellow) and **V** (green) along the inferred trajectory of the spacecraft, referred to the scale shown at top left. The white dot is that place in the structure where the axial component maximizes and the spacecraft passes close to it (i.e., small impact parameter) and can sample the structure well (see below).

Figure 3 shows the residue map, which is a measure of how good this reconstruction is. The circle and star symbols correspond, respectively, to values of P_t when the spacecraft is approaching and receding from the center. The dashed curve gives the fit of the data to a second-order polynomial function with an exponential tail. The fit is seen to be very good, with a residue value of just 0.03. (Values up to 0.2 are often taken as defining a satisfactory fit.) For the orientation, the GS technique gives longitude = 19.86°, latitude = −8.71° (GSE) and impact parameter, p, = −0.047 AU. Compared to values obtained from minimum variance, the longitudes differ by 13° and the latitudes by ∼9°. This good agreement affords further confirmation of the unusual orientation of the MC's axis. Using the duration of spacecraft traversal at the speed of the cloud center yields a distance covered by the spacecraft of 0.344 AU.

3.2. The Sheath Region

We now discuss the sheath region, examining the interval from 12 UT (3) to 0:30 UT (4), that is, from shock wave to the second discontinuity. Here B and N are approximately constant (mean and standard deviation: 9.25 ± 0.25 nT and 3.05 ± 0.57 cm^{-3}, respectively), which is untypical of MC sheaths. Visible also in Figure 1 is a significant rotation when the waves interacted with shock wave. For example, B_y and B_z changed polarity.

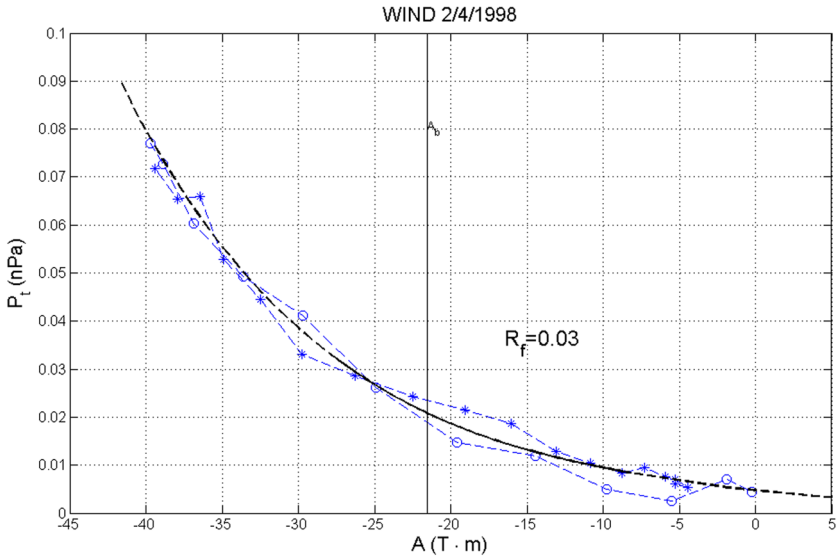

Figure 3. The fitting residue, R_f. The residue plot giving a measure of the goodness of the reconstruction. The circle and star symbols correspond, respectively, to values of P_t while nearing and receding from the closest approach to the axis. The black curve is the fit to the data. The vertical line gives the boundary value of A (labeled A_b) and corresponds to the thick white curve in Figure 2. See text for further details.

Indications are that even before the shock wave, indeed for ~1.5 days earlier, there is a strong correlation between the field and flow components (not shown).

From 6–12 UT (3) the upstream solar wind is predominantly radial and the magnetic field is in a Parker-spiral orientation for a toward sector ($B_x > 0$). Specifically, we have (mean and standard deviation): field: $B_x = 5.9 \pm 0.5$, $B_y = -3.8 \pm 0.9$, $B_z = 1.1 \pm 0.8$ nT; flows: $V_x = -296.0 \pm 8.2$, $V_y = -10.9 \pm 14.2$, $V_z = 30.5 \pm 12.0$ km s^{-1}.

For the interval 12 UT (3) to 2 UT (4), we first search for a good deHoffmann-Teller (HT) frame, that is, one where the convection electric field is very small and consequently the flow is approximately field aligned. This is done by minimizing the convection electric field (Khrabrov & Sonnerup, 1998). We obtain a HT frame

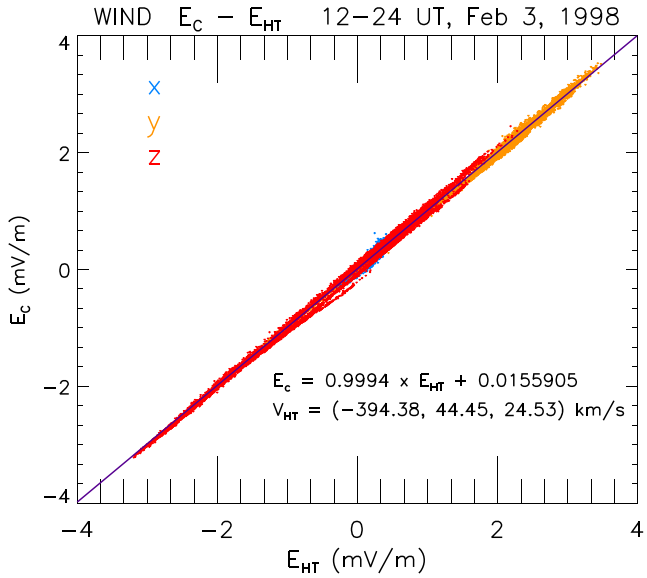

Figure 4. The components of the convection electric field in the GSE frame ($-\mathbf{V} \times \mathbf{B}$) plotted against those of the electric field using the derived HT velocity. The plot indicates that in the derived HT frame the electric field is close to 0 (= 0.016 mV/m).

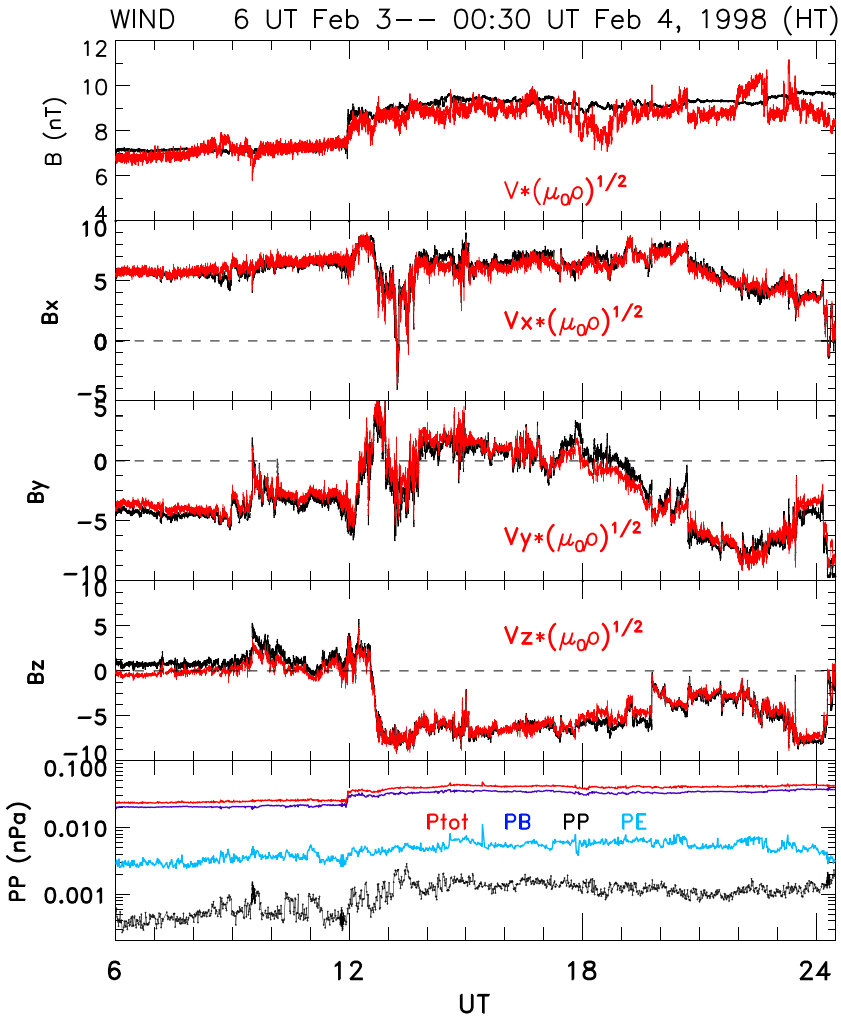

Figure 5. For the indicated 18.5-hr interval, the middle three panels show an overlay of the components of the magnetic field (black) and the velocity components in the HT frame multiplied by $(\mu_0\rho)^{1/2}$ (red), where ρ is the mass density. The top panel shows the total field, and the bottom panel shows the pressures.

velocity $\mathbf{V_{HT}} = (-394.38, 44.45, 24.53)$ km s^{-1} with a correlation coefficient of 0.99935. So we can remove the convection electric field. Since we are in a toward sector, the positive correlation means that the waves are traveling against the field, that is, antisunward, as expected.

In order to check how good this HT frame is, we show in Figure 4 a plot of $\mathbf{E_c} = -\mathbf{V} \times \mathbf{B}$ versus $\mathbf{E_{HT}} = -\mathbf{V_{HT}} \times \mathbf{B}$. The slope is 0.9995 and the residual convection electric field = 0.016 mV/m. In fields of a few mV/m, this residual electric field may be considered small.

In Figure 5 we plot the magnetic field components in black and overlay the flow components in the HT frame in red. The flows have been multiplied by $(\mu_0\rho)^{1/2}$, where ρ is the mass density, so that they are also in units of nT. We note that the variations are large, with amplitude ~8 nT, comparable to the background (i.e., average) field (7.2 nT). Clearly, there is excellent agreement between the black and the red traces. This indicates that we are dealing with large-amplitude Alfvén waves.

We now look at the Alfvén ratio, that is, the kinetic-to-magnetic spectral energy ratio. At 1 AU, the average of the Alfvén ratio is typically 1/2, and this holds for both slow and fast winds (see, e.g., Marsch & Tu, 1990, see their Figure 7; Wang et al., 2012). We computed the velocity and magnetic spectra separately. We converted magnetic to velocity units based on the mean number density (here 3.25 cm^{-3}, taking into account the α particle contribution). In Figure 6 the top panel shows the power spectrum of V (solid trace) and B (dashed trace) in velocity units. Then we evaluated the spectral ratio per frequency. The Alfvén ratio is plotted in

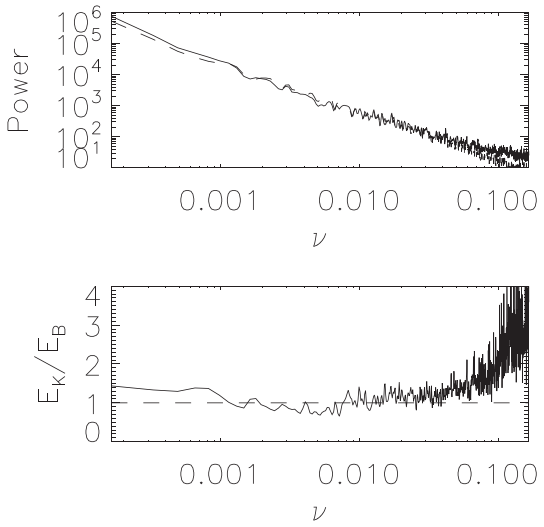

Figure 6. The top plot shows the power spectrum of V (solid lines) and B (dashed) in velocity units plotted as a function of frequency in Hz. Note the rise of the V spectrum at high frequencies, which is probably due to digitization errors on the PESA-low onboard moments. The bottom plot is the ratio of the kinetic-to-magnetic spectral energy, that is, the Alfvén ratio. Below a frequency of 0.07 Hz, the Alfvén ratio is close to unity. We used a mean proton + alpha particle density of 3.25 cm^{-3}.

Figure 6, bottom panel, as a function of frequency in Hz. In our case, equipartition (ratio = 1) was found for a wide range of frequencies. This result lends further support to the conclusion that we are dealing with LAAWs, where equipartition should be present (Matthaeus & Goldstein, 1982). In summary, we have a long MC sheath consisting of LAAWs.

We now direct attention to the shock wave-like feature at ~11:58 UT (3). We first carry out a minimum variance analysis on the high-resolution (~11 Hz) **B** field data from *Wind*, choosing the interval 11:52 to 12:02 UT (3) for the analysis. We obtain the normal **N** = (0.91, −0.39, −10). The intermediate-to-minimum eigenvalue ratio = 5.7. We then use the coplanarity theorem (Abraham-Shrauner, 1972) and obtain a shock normal **N** = (0.92, −0.36, −0.14) and a shock speed of 322.8 km/s. The angle between the normals from these two methods is only 3°. The angle the normal makes with the upstream field, $\theta_{BN} = 20.4°$ so we are dealing with a quasi-parallel and weak shock-like structure.

Figure 7 shows the time profiles of the **B** and **V** vectors in minimum variance coordinates, *ijk*, where (*ij*) represents the shock plane. As expected, there are plenty of waves just upstream of the shock wave feature. The field and flow fluctuations in the (ij) plane are related, with correlation coefficients of 0.96 and 0.87, respectively, while those in the **k** direction are not. So we conclude that the Alfvén waves impinging on the parallel shock wave are "channeled" to oscillate parallel to the shock surface.

3.3. The Interaction Region

Magnetic field and proton data for the time when the LAAWs approach the MC boundary are shown in Figure 8. (We shall call this inner sheath region the interaction region.) The blue traces in Panels 2–4 give the GSE components of the velocity. The bottom panel shows the total β. Throughout, the total pressure (red trace in the last-but-one panel) remains practically constant (= 0.04 ± 0.003 nPa). Two prominent discontinuities (DDs) are evident at times of the first two vertical guidelines. At 00:10 UT (4) (dashed blue guideline) the field and flow components change and total bulk speed increases, while total field remains constant. A second DD occurs at ~2:30 UT (4). It marks the start of a ~2-hour period where a magnetic depression occurs. At 4:32 UT (4) the magnetic field strength rises suddenly, the density drops, and the velocity and temperature increase. These signatures taken together characterize a slow expansion fan (Sanchez et al., 1990). For ease of description, we label the regions between the DDs as R1 and R2. The slow expansion fan which follows R2 marks the beginning of the MC.

To understand regions R1 and R2 better, we now consider the electron behavior. This we do in two complementary figures. The first is Figure 9, using the new analysis technique mentioned in section 2

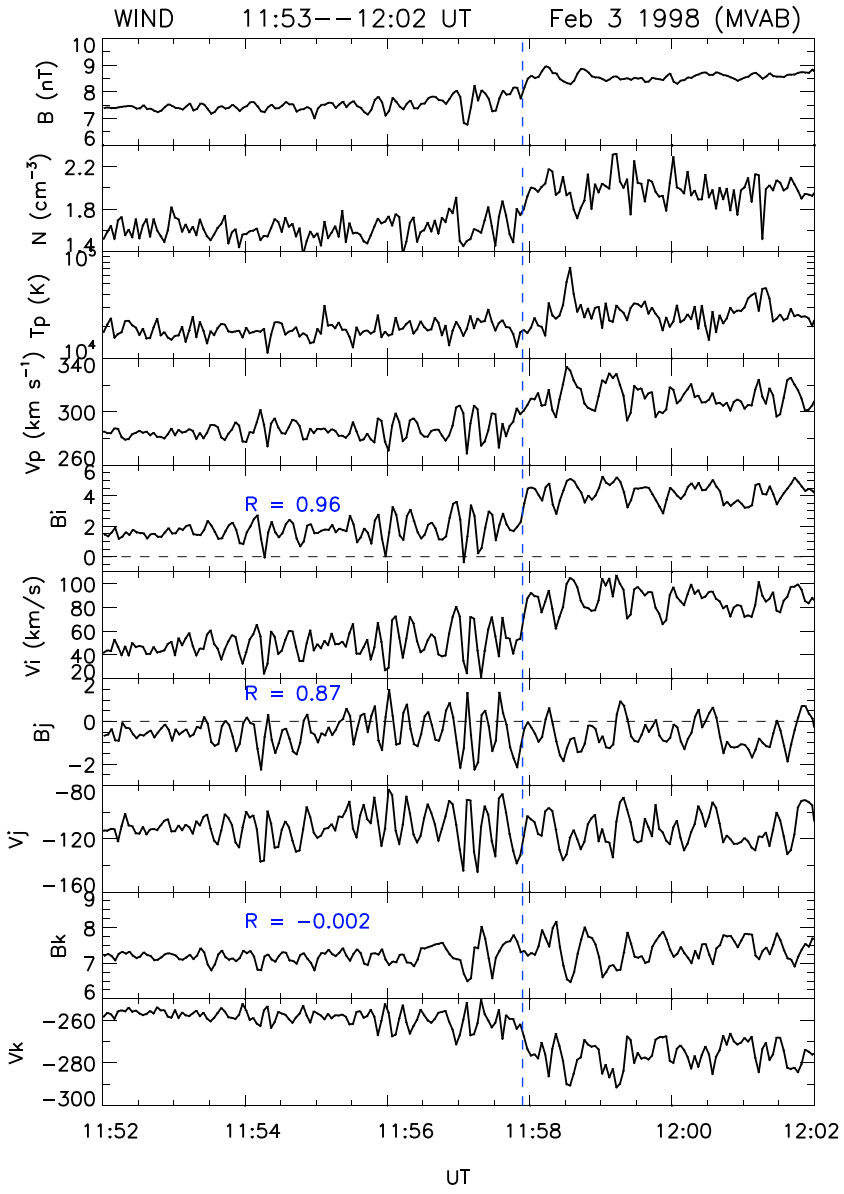

Figure 7. For the 10-min interval 11:52–12:02 UT (3), the plot shows the total field strength, the proton density, temperature and bulk speed, and (pairwise) the components of the field and flow vectors in minimum variance coordinates (*ijk*). The nominal shock front is at 11:58 UT (vertical guideline).

(Wilson III et al., 2019a). From top to bottom the figure shows the total electron density and, overlaid in blue, the effective electron temperature. Then follow the (three-point smoothed) density and temperature (in blue) of the halo component, the density and temperature (in blue) of the strahl component, the y component of the electron velocity and overlaid in red the z component (GSE), and in the last panel the total flow speed in black and the x component of the flow in blue. We modeled electron VDFs by the sum of three model functions, one each for the core, the halo, and the field-aligned strahl. The cold dense core is best fit with either a bi-kappa or a bi-self-similar VDF, either symmetric or asymmetric. The halo and strahl are best fitted with a bi-kappa VDF. We note that the effective electron temperature is defined as the sum of the density multiplied by the temperature of the three components of the electron VDF divided by the sum of their densities ($\Sigma_j(n_jT_j)/\Sigma n_j$ where j = core, halo, strahl). The complementary figure (Figure 10) shows the electron pitch angle distributions at three energies, from top to bottom, 634.4, 292.0, and 136.8 eV during the time interval 1:45 to 5:30 UT (4). For reasons discussed below, a longer interval showing the behavior of the VDFs during the first discontinuity is shown in Figure 11.

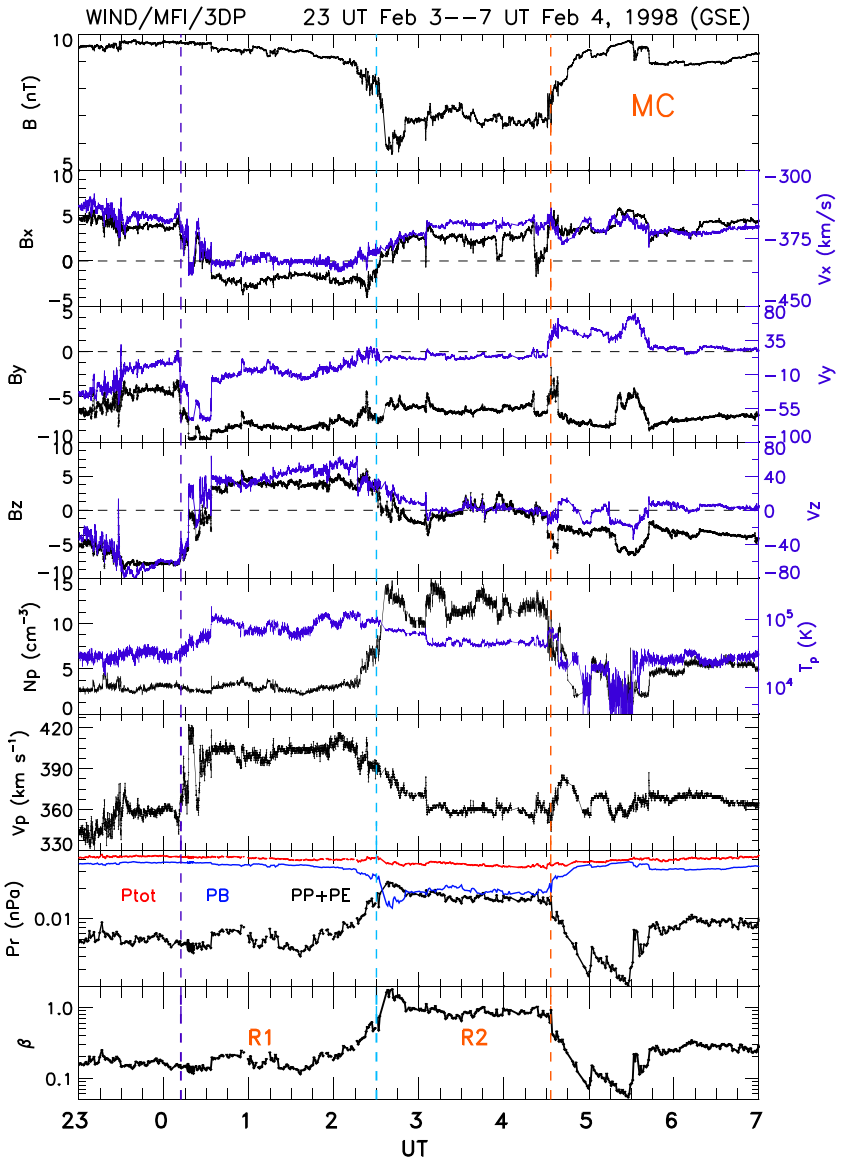

Figure 8. For an 8-hr interval preceding and including the front boundary of the MC, the figure displays from top to bottom the total field and its GSE components (overlaid in blue, the corresponding flow vector components), an overlay of the total density (black trace) and the proton temperature (blue), the flow speed, the pressures and the total plasma β. The first two vertical guidelines are drawn at two field and flow discontinuities discussed in the text. The leading edge of the MC is at the time of the last vertical guideline.

At the first DD we performed a stress balance test (Walén; Paschmann et al., 1986; Sonnerup et al., 1981). The results are shown in Figure 12, which plots the theoretically expected ion velocity changes for a 2-D, static rotational discontinuity versus the observed ones. With cross-correlation coefficients, $R_i = 1.0$, and slopes of 1.0, 0.8, 1.0, the agreement between the predicted and observed velocity changes is excellent. This, together with the accelerated flow burst—in both ions and electrons—indicates that reconnection is ongoing, and we have here a reconnecting current sheet (rotational discontinuity). The flow burst is taking place at a field-reversal region: the B_x and B_z components change polarity at this rotational discontinuity: B_x (B_z) go from positive (negative) to negative (positive). This change in magnetic topology indicates a cutting of field lines at the reconnection site. At this time, Figure 11 shows that the 180° PA strahl electron flux suffers a sharp cut. This is because as a result of reconnection the field lines have severed their connection to the Sun. (Note the different scales in Figures 10 and 11.) Disconnection from the Sun is seen as well in the factor of more than 200 drop in the strahl density (Figure 9, Panel 4).

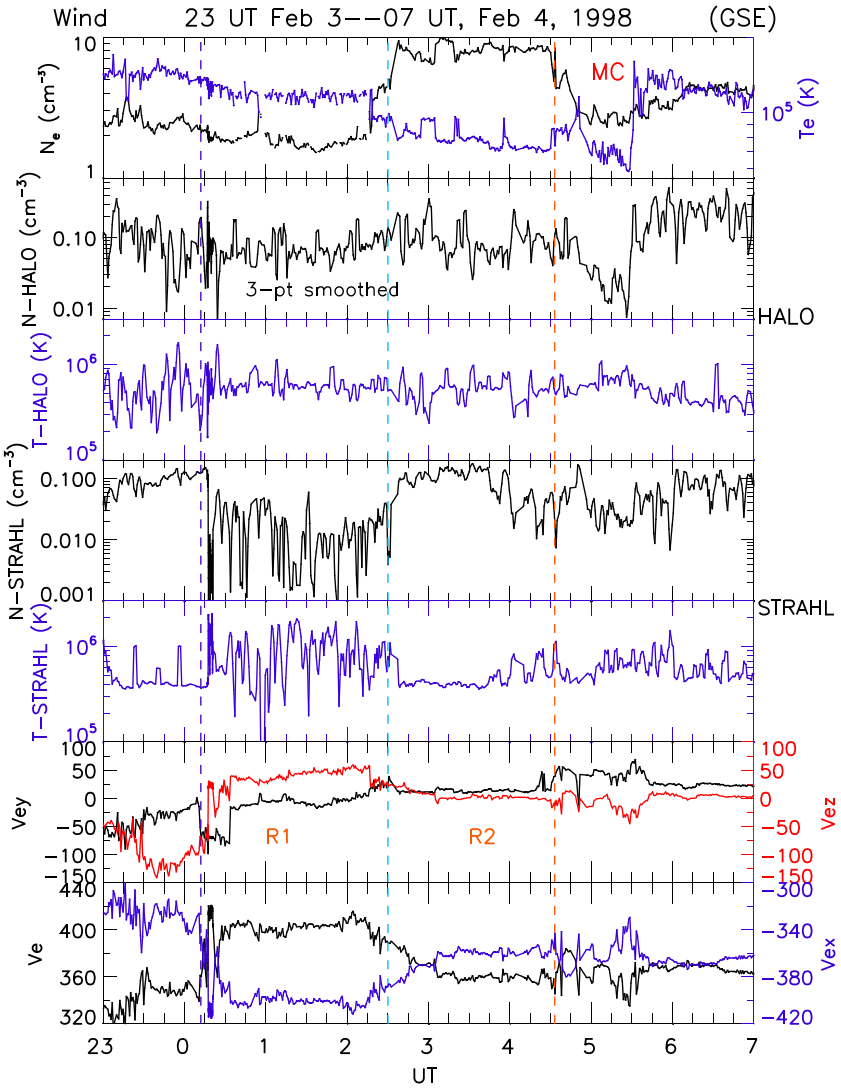

Figure 9. Details on the behavior of the electrons for the same interval as in the previous figure. From top to bottom we have the total density and, in blue, the effective total temperature, the density and temperature of the halo (second and third panels) and of the strahl (fourth and fifth panels), and velocity components and the total flow speed. The marked regions are the same as those in Figure 8.

At the second DD, when the magnetic field strength suddenly drops, B_x reverts to positive values (typical of a toward sector) and B_z ~0 nT (Figure 8). Here the strahl is bidirectional and strong. Toward the end of R2, from 4 UT onward, the bidirectionality is intermittently disrupted. We have here a mixture of closed and open field lines. Note in Figures 8 and 9 how the Y and Z components of the ion and electron flow vectors are nearly zero in R2.

The interval ends in a slow expansion fan. Here B increases, N decreases, and T and V increase. We suggest this to be the front boundary of the MC. Downstream of it, the magnetic fields strength rises steeply and the plasma density drops precipitously. Figure 10 shows a wholesale depletion of the halo electrons at 90° PA and continued, episodic disruptions of the strahl bidirectionality. Thus, Figure 9 shows in the second panel the halo density going down just after entry into the MC. Because the halo component is hot, its disappearance leads to a concomitant drop in the total temperature (blue trace in top panel) in addition to a drop in the core temperature (not shown). The behavior of the strahl implies a sequence of open and closed field lines. We now turn to discuss these features below.

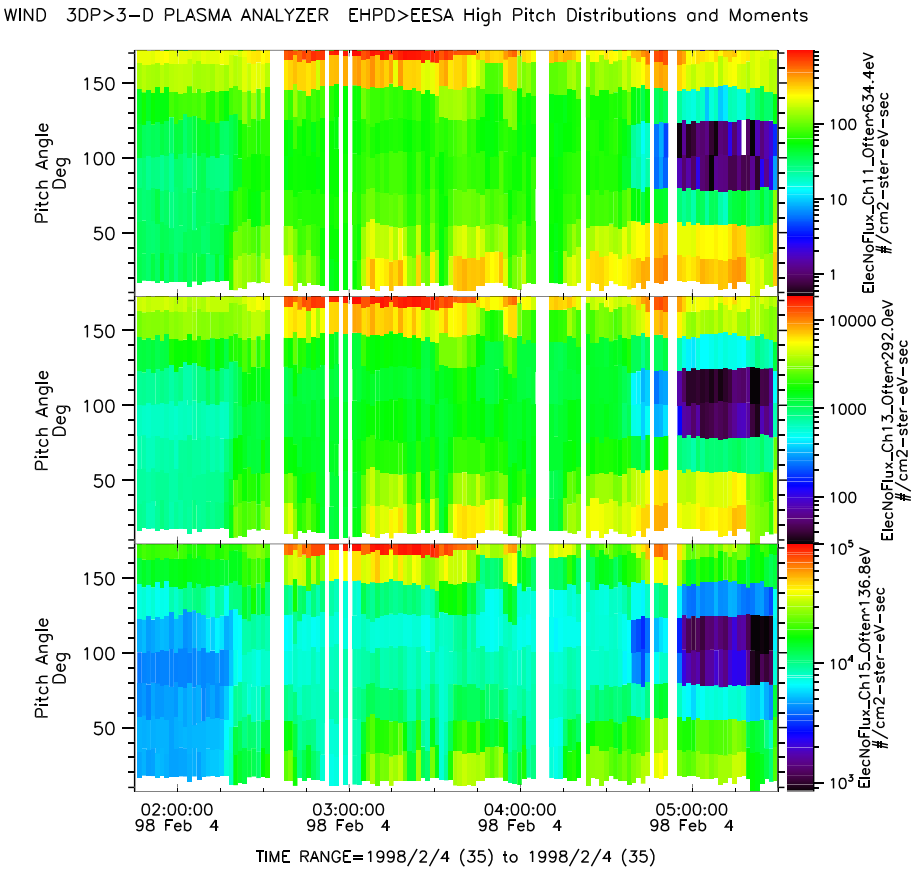

Figure 10. Pitch angle (PA) distributions of suprathermal electrons (from top: 634.4, 292.0, and 136.8 eV) taken from the 3DP instrument. The interval when the field is depressed (~2:30 – ~4:30 UT) contains sporadic interruptions of bidirectional flows. For contrast, we include an earlier and a later interval. In the earlier time segment (1:45–02:30 UT) the streaming is opposite to the field direction (PA = 180°). The later interval occurs after the slow expansion fan. It shows a pronounced depletion of the halo population around 90° PA, also seen in Panel 2 of the preceding figure.

4. Discussion and Conclusions

We have presented observations acquired by spacecraft *Wind* of large-amplitude Alfvén waves appearing for several hours before, and populating the sheath region of, a slow MC, and interacting with the transient. The approach we adopted was similar to that of Wang et al. (2012). These authors presented a ~25-min period where LAAWs were present in the fast solar wind at 1 AU. The relation between the field and flow fluctuations was done in the HT frame. They found an Alfvén ratio of ~1 (>0.98) in the frequency range $f < 10^{-2} Hz$. There are several similarities with our results, such as the frequency range when the Alfvén ratio ≈1 (Figure 6). Our work has, however, an entirely different context. Main differences are as follows: (i) the observations of LAAWs were made in the slow wind, (ii) they lasted much longer, (iii) we also included interaction of the waves with a large solar wind transient structure in association with which they occur, and (iv) importantly, we applied a state-of-the-art analysis technique on electron VDFs.

We noted that the plasma beta rose considerably in the later part of the transient event and approached unity. The designation "MC" might thus not be the best in this case since the definition stipulates a low β_p (Burlaga et al., 1981). However, this has little impact on the aim of this work. Incidentally, using practically the same duration (4 UT (4) to 23 UT (5)), Richardson and Cane (2010) classify this transient as a reported MC (their Table 1).

The MC was unusually oriented. To find the axis, we applied a minimum variance analysis to the magnetic field data and used the eigenvector corresponding to the maximum variance direction. This departs from the usual convention of using the intermediate eigenvector for the axis (Goldstein, 1983). Goldstein's work targeted, however, force-free flux ropes, which is not what we have here. Xiao et al. (2004) (see also Fear

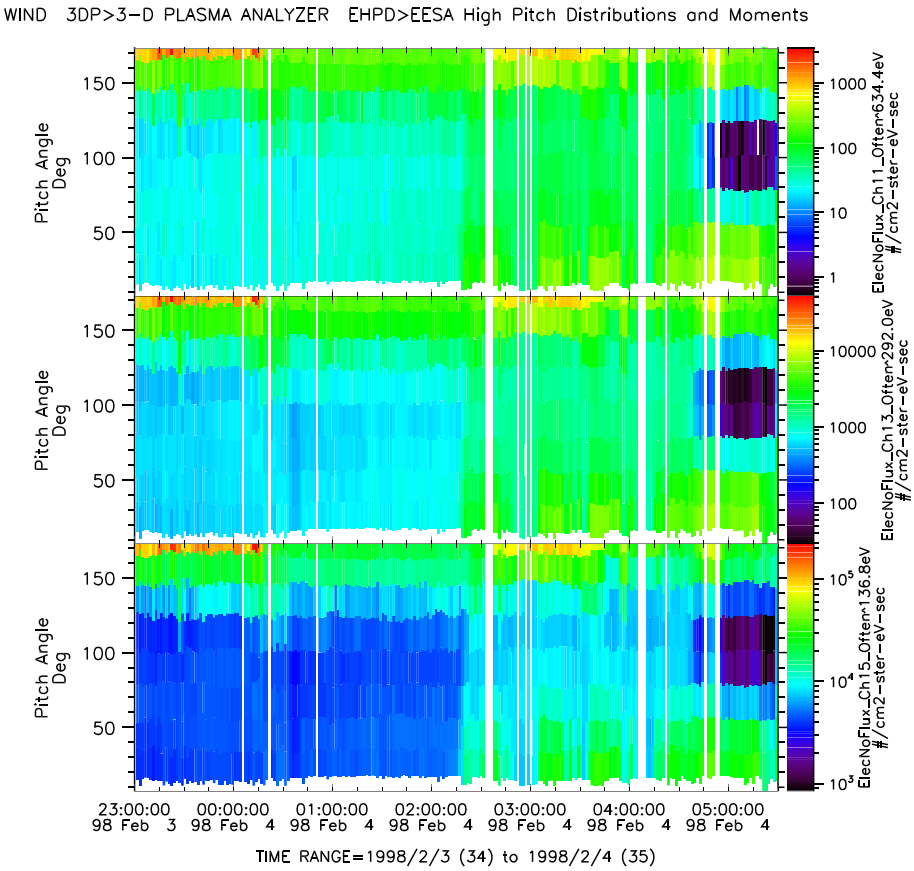

Figure 11. Similar to the previous figure but starting from 23 UT (2) to highlight the abrupt interruption of the 180° strahl at the rotational discontinuity at ~0:16 UT (4).

et al., 2009) noted that when using minimum variance of the magnetic field data, which eigenvector to use for the axis depends on the spacecraft path relative to the flux rope. For force-free cases they came to the same conclusion as Goldstein (1983). For nonforce - free ropes, if the spacecraft cuts through a strong core field then it was argued that the maximum eigenvector could be taken as the axis direction. In our case, this choice was confirmed by GS reconstruction, a technique that does not presuppose force-free conditions.

Two qualifications are in order here. The first is that the MC could actually have resulted from a merger of two MCs, similar to the cases discussed by Dasso et al. (2009) and Lugaz and Farrugia (2014). If so, this might then explain the unusual orientation. However, careful analysis of the in situ measurements of this event resulted in our discarding this possibility. We also note that all the interplanetary coronal mass ejection (ICME) databases list this as a single MC. The second is that since the MC is expanding the Grad-Shafranov reconstruction results should be considered with care. A measure of its reliability is the ratio of the radial expansion speed, Vexp, to the average Alfvén speed, $< V_A >$: the smaller the ratio, the better. In our case, this ratio = 0.38, so that the underlying static assumption is moderately well satisfied.

The interaction region (i.e., the inner sheath) contains some interesting and intriguing aspects. The field and flow behaviors suggest a layered structure (labeled R1–R2), and the approach of the LAAWs to the ejecta seems to be mediated by two discontinuities. At the first discontinuity magnetic reconnection is taking place. The associated cutting of the interplanetary magnetic field lines leads to a disappearance of the electron strahl component (Figure 9, fourth panel, and Figure 11). Figure 13a shows this through the electron VDF at 1:44:20 UT, presented as contours of constant phase space density. The X and Y axes give the flow parallel and perpendicular, respectively, to the magnetic field, indicated by the red arrow. The energetic components parallel and anti-parallel to the field are missing. We note that similar discontinuous features have been found in other sheaths, which have generally much lower Alfvénicity; in the case we have examined, we

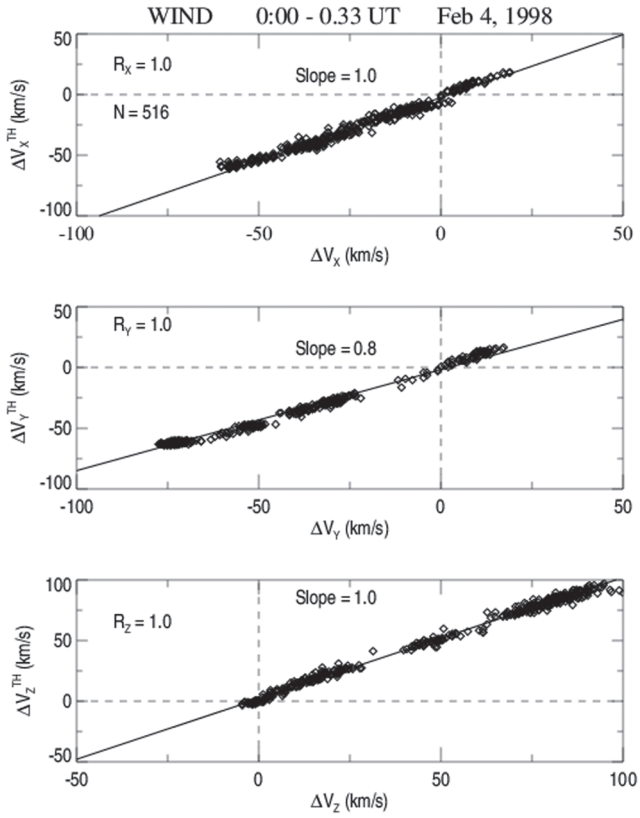

Figure 12. Result of a Walén test for the first discontinuity. Expected changes in the velocity components are plotted against the corresponding observed values.

postulate that the unusually high Alfvénicity is an important factor in the formation of the discontinuities present.

A 2-hour-long magnetic field decrease follows (R2). Here (i) the electron and ion densities increase and pressure balance is maintained, (ii) the Y and Z components of the velocities go to 0; (iii) the strahl reinstates itself and reaches the highest densities in the interval, (iv) it is generally bidirectional, at least in the energies 292 and 634 eV, but with intermittent disruptions particularly from 4 UT (4) till the end of region R2. This signifies a mixture of field lines connected and disconnected from the Sun. The origin of R2 may be explained as a noncompressive density enhancement that envelops the MC and so shields it from direct contact with the sheath and the LAAWs. This prevents the LAAWs from eroding the cloud through intermittent reconnection, which is likely to occur when Alfvén waves impinge on a closed magnetic field boundary. Noncompressive density enhancements are cases where the density is elevated but the temperature goes down and the speed is constant or falling. This would not happen if one compresses the plasma. These structures have been associated with crossings of the heliospheric current sheet (Borrini et al., 1981; Gosling et al., 1977).

As the spacecraft crosses into the MC, from 4:30–5:30 UT (4) there is a strong positive gradient in the magnetic field and simultaneously the density drops sharply by over a factor of 3. As a consequence, the plasma β attains its lowest values. This region is marked by a clear depletion of the electron halo component roughly symmetric about 90°(Figures 9 and 10). (We note that there no further halo depletions till the end of the MC. However, the strahl in the MC is bidirectional with random interruptions.) Figure 13b shows contours of constant phase space density (in cm^{-3} km^{-3} s^3) of a 2-D cut through the 3-D electron VDF during the period 05:00:25.401–05:00:28.403 UT (4). In this plot the horizontal axis is $V_{||}$ to the background field and the vertical axis is $V_{\perp}$. The purple arrow shows the bulk velocity vector and the red is in the direction of the Sun. There is a clear "erosion" (flattening) of the phase space densities in directions at large angles to the background field. This is the halo depletion. Contrast this with Figure 13a for ~01:44:18 UT (4), representing a dropout of the parallel strahl component (see above).

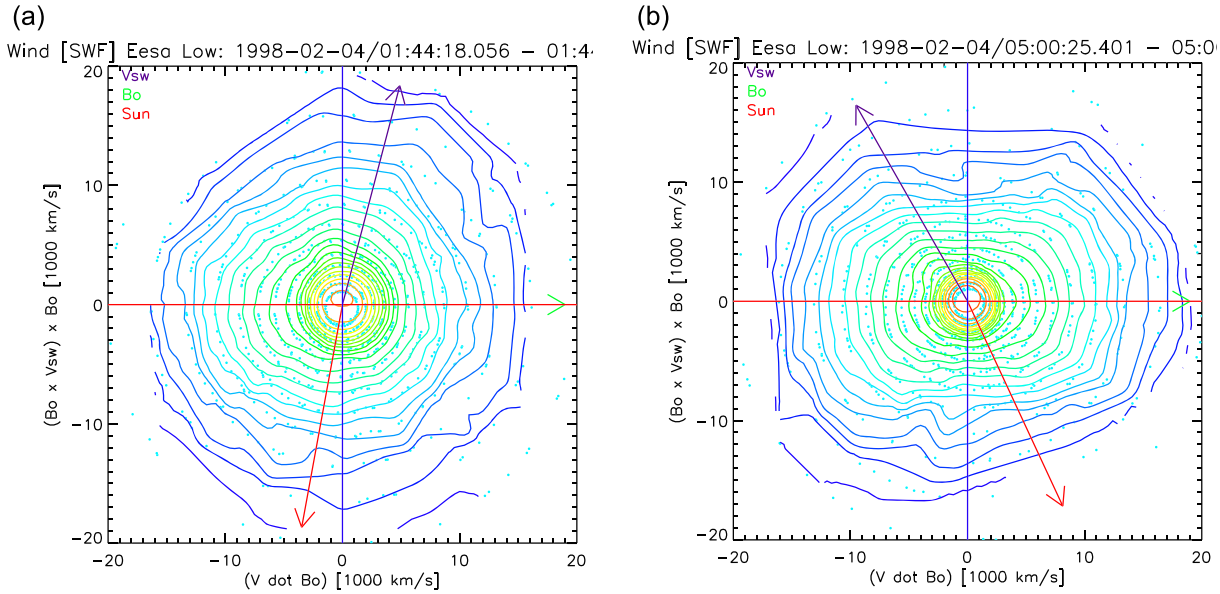

Figure 13. (a) Electron velocity distribution function during a time of strahl drop-out at 1:44:20 UT (R1). The ordinate gives the flow velocity perpendicular to the magnetic field and the abscissa the flow velocity parallel to the magnetic field. The red arrow is the sunward direction and the purple arrow gives the average direction of the bulk flow speed during this time. (b) Similar to panel a, but this time showing the electron VDF during a halo depletion (R3).

Electron halo depletions on open or closed field lines are believed to result from mirroring and focusing in magnetic field enhancements (Gosling et al., 2001, 2002; Skoug et al., 2006). There are indeed sharp field gradients in this interval though we cannot pin down the exact cause of this depletion.

With the presence of a rotational discontinuity followed by a slow expansion fan in the inner sheath region, we cannot resist drawing an analogy with a reconnecting magnetopause in the Levy et al. (1964) model. There these two discontinuities occurring in this same order in an inbound crossing are postulated to be necessary to affect the transition of the magnetic field and plasma from the inner magnetosheath to the terrestrial magnetosphere for a southward pointing IMF B_z, thus enabling reconnection. The region in between these two discontinuities would constitute the boundary layer. Similar ideas were advanced by Siscoe and Sanchez (1987) to describe the transition through the high latitude boundary layer, that is, the plasma mantle. On a kinetic physics description of the ion diffusion region, these two discontinuities appear as a rotational discontinuity and a stagnation line (Cassak & Shay, 2007). We may thus think of regions R1 and R2 as constituting a boundary layer of the MC. We would thus apply physics in a planetary context to a different heliospheric regime. We note that the comparison of MC and planetary sheaths is the focus of the work by Siscoe and Odstrcil (2008).

As this work was being made ready for submission, a paper appeared which considers Alfvén waves in an ICME sheath (Shaikh et al., 2019). The authors note that "in general CME-sheath does not exhibit Alfvénic characteristics. This type of event is unique or rare to observe." The paper focuses on the co-existence of a planar magnetic structures and Alfvén waves in the sheath region of an MC, arguing that an instability at the planar magnetic structure gave rise to the waves. The speed of the sheath in their example was (borderline) high, unlike that in the event we studied. In our case, the Alfvén waves were not created locally; we see them also outside the MC.

To conclude, large-amplitude Alfvén waves, which are typically found in fast streams, are seen here in conjunction with a slow transient. By causing reconnection at the terrestrial magnetopause, thereby eroding the front boundary of the magnetospheric obstacle, Alfvén waves are one main cause of geoeffects at Earth. In our example we may also think of the MC as an obstacle to the Alfvén waves. Yet in this case these waves do not erode this obstacle.

Data Availability Statement

Solar wind data from the *Wind* spacecraft are obtained online (http://cdaweb.gsfc.nasa.gov/istp_public/).

Acknowledgments
This work was supported by NASA Grants 80NSSC19K1293, NNX16AO04G, 80NSSC20K0197, 499878Q, 499935Q, NNX15AB87G, and 80NSSC19K0832 and NSF Grant AGS-1435785. This work was supported by the International Space Science Institute's (ISSI) International Teams program. L. V. W. was partially supported by *Wind* MO&DA funds and a Heliophysics Innovation Fund (HIF).

References

Abraham-Shrauner, B. (1972). Determination of magnetohydrodynamic shock normals. *Journal of Geophysical Research*, *77*, 736.

Belcher, J. W., & Davis Jr, L. (1971). Large-amplitude Alfvén waves in the interplanetary medium, 2. *Journal of Geophysical Research*, *76*, 3534.

Borrini, G., Gosling, J. T., Bame, S. J., Feldman, W. C., & Wilcox, J. M. (1981). Solar wind helium and hydrogen structure near the heliospheric current sheet: A signal of coronal streamers at 1 A.U. *Journal of Geophysical Research*, *86*, 4565.

Burlaga, L, Sittler, E., Mariani, F., & Schwenn, R. (1981). Magnetic loop behind an interplanetary shock: Voyager, Helios, and IMP8 observations. *Journal of Geophysical Research*, *86*, 6673–6684.

Cassak, P. A., & Shay, M. (2007). Scaling of asymmetric magnetic reconnection: General theory and collisional simulations. *Physics of Plasmas*, *14*(102114).

Chao, J. K., Hsieh, W.-C., Yang, L., & Lee, L. C. (2014). Walén test and De Hoffmann-Teller frame of interplanetary large-amplitude Alfvén waves. *The Astrophysical Journal*, *786*, 149. https://doi.org/10.1088/0004-637X/786/2/149

Dasso, S., Mandrini, C. H., Schmieder, B., Cremades, H., Cid, C., Cerrato, Y., et al. (2009). Linking two consecutive nonmerging magnetic clouds with their solar sources. *Journal of Geophysical Research*, *114*, A02109. https://doi.org/10.1029/2008JA013102

deHoffmann, F., & Teller, E. (1950). Magnetohydrodynamic shocks. *Physical Review A*, *80*, 692.

Démoulin, P., Nakwacki, M. S., Dasso, S., & Mandrini, C. H. (2008). Expected in situ velocities from a hierarchical model for expanding interplanetary coronal mass ejections. *Solar Physics*, *250*, 34.

Farrugia, C. J., Burlaga, L. F., & Lepping, R. P. (1997). Magnetic Clouds and the quiet/storm effect at Earth: A review. In B. T. Tsurutani, W. D. Gonzalez, Y. Kamide, & J. K. Arballo (Eds.), *Magnetic storms, Geophysical Monograph Series* (Vol. 98, pp. 91). Washington, DC: American Geophysical Union.

Farrugia, C. J., Burlaga, L. F., Osherovich, V. A., Richardson, I. G., Freeman, M. P., Lepping, R. P., & Lazarus, A. (1993). A study of an expanding interplanetary magnetic cloud and its interaction with the Earth's magnetosphere: The interplanetary aspect. *Journal of Geophysical Research*, *98*, 7621.

Farrugia, C. J., Erkaev, N. V., Jordanova, V. K., Lugaz, N., Sandholt, P. E., Mühlbachler, S. M., & Torbert, R. B. (2013). Features of the interaction of interplanetary coronal mass ejections/magnetic clouds with the Earth's magnetosphere. *Journal of Atmospheric and Terrestrial Physic*, *99*, 1426.

Fear, R. C., Milan, S. E., Fazakerley, A. N., Formacon, K.-H., Carr, C. M., & Donduras, I. (2009). Simultaneous observations of flux transfer events by THEMIS, Cluster, Double Star, and superDARN: Acceleration of FTEs. *Journal of Geophysical Research*, *114*, A10213. https://doi.org/10.1029/2009JA014310

Feldman, W. C., Asbridge, J. R., Bame, S. J., Montgomery, M. D., & Gary, S. P. (1975). Solar wind electrons. *Journal of Geophysical Research*, *80*, 4181.

Goldstein, H. (1983). On the field configuration in magnetic clouds. Solar Wind Five, NASA Conf. Publ,. 228, 731.

Gosling, J. T., Hildner, E., Asbridge, J. R., Bame, S. J., & Feldman, W. C. (1977). Noncompressive density enhancements in the solar wind. *Journal of Geophysical Research*, *82*, 5005.

Gosling, J. T., Skoug, R. M., & Feldman, W. C. (2001). Solar wind electron halo depletions at 90° angle. *Geophysical Research Letters*, *28*(22), 4155.

Gosling, J. T., Skoug, R. M., Feldman, W. C., & McComas, D. J. (2002). Symmetric suprathermal electron depletions on closed field lines in the solar wind. *Geophysical Research Letters*, *29*(12), 1573. https://doi.org/10.1029/2001GL013949

Gulisano, A. M., Démoulin, P., Dasso, S., Ruiz, M. E., & Marsch, E. (2010). Global and local expansion of magnetic clouds in the inner heliosphere. *Astronomy & Astrophysics*, *509*, A39. https://doi.org/10.1051/0004-6361/200912375

Heinemann, S. G., Temmer, M., Farrugia, C. J., Dissauer, K., Kay, C., Wiegelmann, T., et al. (2019). CME-HSS interaction from Sun to Earth. *Solar Physics*, *294*, 121.

Hu, Q., & Sonnerup, B. U. (2001). Reconstruction of magnetic flux ropes in the solar wind. *Geophysical Research Letters*, *28*, 467.

Hu, Q., & Sonnerup, B. U. (2002). Reconstruction of magnetic clouds in the solar wind: Orientations and configurations. *Journal of Geophysical Research*, *107*, 1142. https://doi.org/10.1029/2001JA000293

Khrabrov, A. V., & Sonnerup, B. U. O. (1998). *DeHoffmann - Teller Analysis. Analysis methods for multi-spacecraft data*. In G. Paschmann, & P. W. Daly (Vol. 9, pp. 221–248). Bern, Switzerland: International Space Science Institute.

Lepping, R. P., Acũna, M. H., Burlaga, L. F., Farrell, W. M., Slavin, J. A., Schatten, K. H., et al. (1995). The wind magnetic field investigation. *Space Science Reviews*, *71*, 207.

Levine, R. H., Altschuler, M. D., & Harvey, J. W. (1977). Solar sources of interplanetary magnetic field and solar wind. *Journal of Geophysical Research*, *82*(7), 1061.

Levy, R. E., Petschek, H. E., & Siscoe, G. L. (1964). Aerodynamic aspects of magnetospheric flow. *AIAA Journal*, 2.

Lin, R. P., Anderson, K. A., Ashford, S., Carlson, C., Curtis, D., Ergun, R., et al. (1995). A three-dimensional plasma and energetic particle investigation for the wind spacecraft. *Space Science Reviews*, *71*, 125.

Lopez, R. E. (1987). Solar wind invariance in solar wind proton temperature relationships. *Journal of Geophysical Research*, *92*(11), 189.

Lugaz, N., & Farrugia, C. J. (2014). A new class of complex ejecta resulting fron the interaction of two CMEs and its expected geo-effectiveness. *Geophysical Research Letters*, *41*, 769–776. https://doi.org/10.1002/2013GL058789

Marsch, E., & Tu, C.-Y. (1990). On the radial evolution of MHD turbulence in the inner heliosphere. *Journal of Geophysical Research*, *95*, 8211.

Matthaeus, W. H., & Goldstein, M. L. (1982). Measurement of the rugged invariants of magnetohydrodynamic turbulence in the solar wind. *Journal of Geophysical Research*, *87*, 6011.

Ogilvie, K. W., Chornay, D. J., Fritzenreiter, R. J., Hunsaker, F., Keller, J., Lobell, J., et al. (1995). SWE, A comprehensive plasma instrument for the wind spacecraft. *Space Science Reviews*, *71*(1-4), 55–77. https://doi.org/10.1007/BF00751326

Paschmann, G., Papmastorakis, I., Baumjohann, W., Sckopke, N., Carlson, C. W., Sonnerup, B. U. Ö., & Lühr, H. (1986). The magnetopause for large magnetic shear: AMPTE/IRM observations. *Journal of Geophysical Research*, *91*, 11,099.

Richardson, I. G., & Cane, H. V. (2010). Near-Earth interplanetary coronal mass ejections during solar cycle 23 (1996-2009): Catalog and summary of properties. *Solar Physics*, *264*, 189–237. https://doi.org/10.1007/s11207-010-9568-6

Rosenbauer, H., Schwenn, R., Marsch, E., Meyer, B., Miggenrieder, H., Montgomery, M. D., et al. (1977). A survey on initial results of the HELIOS plasma experiment. *Journal of Geophysics*, *42*, 561.

Sanchez, E., Siscoe, G. L., Gosling, J. T., Hones Jr, E., & Lepping, R. P. (1990). Observations of rotational discontinuity-slow expansion fan structure of the magnetotail boundary. *Journal of Geophysical Research*, *A1*, 61–73.

Shaikh, Z. I., Raghav, A., & Vichare, G. (2019). Coexistence of a planar magnetic structure and an Alfv/'en wave in the shock-sheath of an interplanetary coronal mass ejection. *Monthly Notices of the Royal Astronomical Society*, *490*, 1638–1643. https://doi.org/10.1093/mnras/stz2743

Siscoe, G., & Odstrcil, D. (2008). Ways in which ICME sheaths differ from magnetosheaths. *Journal of Geophysical Research*, *113*, A00B07. https://doi.org/10.1029/2008JA013142

Siscoe, G. L., & Sanchez, E. (1987). An MHD model for the complete open magnetotail boundary. *Journal of Geophysical Research*, *92*, 7405–7412.

Skoug, R. M., Gosling, J. T., McComas, D. J., Smith, C. W., & Hu, Q. (2006). Suprathermal electron 90° angle depletions at reverse shocks in the solar wind. *Journal of Geophysical Research*, *111*, A01101. https://doi.org/10.1029/2005JAJA011316

Sonnerup, B. U. Ö., Paschmann, G., Papmastorakis, I., Sckopke, N., Haerendel, G., Bame, S. J., et al. (1981). Evidence for magnetic reconnection at the Earth's magnetopause. *Journal of Geophysical Research*, *86*, 10,049.

Sonnerup, B. U., & Scheible, M. (1998). Minimum and maximum variance analysis. In G. Paschmann, & P. W. Daly (Eds.), *Analysis methods for multi-spacecraft data* (Vol. 8, pp. 185–220). Bern, Switzerland: International Space Science Institute.

Sturrock, P. A. (1994). *Plasma physics: An introduction to the theory of astrophysical geophysical and laboratory plasmas*. UK: Cambridge University Press.

Wang, X., He, J., Tu, C., Marsch, E., Zhang, L., & Chao, J.-K. (2012). Large-amplitude Alfvé,n wave in interplanetary space: The Wind spacecraft observations. *The Astrophysical Journal*, *746*, 147. https://doi.org/10.1088/0004-637X/746/2/147

Wilson III, L. B., Chen, L-J., Wang, S., Schwartz, S. J., Turner, D. R., Stevens, M. L., et al. (2019a). Electron energy partition function across interplanetary shocks. I. Methodology and data product. *The Astrophysical Journal Supplement Series*, *243*, 8. https://doi.org/10.3847/1538-4365/ab22bd

Wilson III, L. B., Chen, L.-J., Wang, S., Schwartz, S. J., Turner, D. L., Stevens, M. L., et al. (2019b). Electron energy partition function across interplanetary shocks. II. Statistics. *The Astrophysical Journal Supplement Series*, *245*(2), 24. https://doi.org/10.3847/1538-4365/ab5445

Xiao, C. J., Pu, Z. Y., Ma, Z. W., Fu, S. Y., Huang, Z. Y., & Zong, Q. C. (2004). Inferring of flux rope orientation with the minimum variance analysis technique. *Journal of Geophysical Research*, *109*, A11218. https://doi.org/10.1029/2004JA010594